Title

Open-channel metal particle superlattices

Journal

Nature, 611(7937)

ISSN

0028-0836

Authors

Li, Yuanwei

Zhou, Wenjie

Tanriover, Ibrahim

et al.

Publication Date

2022-11-24

DOI

10.1038/s41586-022-05291-y

Open Channel Metal Particle Superlattices

Yuanwei Li[1,2], Wenjie Zhou[2,3*], Ibrahim Tanriover[2,4*], Wisnu Hadibrata[2,4], Benjamin E. Partridge[2,3], Haixin Lin[2,3], Xiaobing Hu[5], Byeongdu Lee[6], Jianfang Liu[7], Vinayak P. Dravid[2,5**], Koray Aydin[2,4**], and Chad A. Mirkin[1,2,3**]*

[1]Department of Chemical and Biological Engineering, Northwestern University, Evanston, IL 60208, USA.

[2]International Institute for Nanotechnology, Northwestern University, Evanston, IL 60208, USA.

[3]Department of Chemistry, Northwestern University, Evanston, IL 60208, USA.

[4]Department of Electrical and Computer Engineering, Northwestern University, Evanston, IL 60208, USA.

[5]Department of Materials Science and Engineering, Northwestern University, Evanston, IL 60208, USA.

[6]X-ray Science Division, Advanced Photon Source, Argonne National Laboratory, Lemont, IL, USA

[7]The Molecular Foundry, Lawrence Berkeley National Laboratory, Berkeley, CA 94720, USA.

[*]These authors contributed equally to this work.

[**]Correspondence to: chadnano@northwestern.edu; aydin@northwestern.edu; v-dravid@northwestern.edu

Summary Paragraph

Although tremendous advances have been made in preparing porous crystals from molecular precursors[1,2], there are no general ways of designing and making topologically diversified porous colloidal crystals over the 10-1000 nm length scale. Control over porosity in this size range would enable the tailoring of molecular absorption and storage, separation, chemical sensing, catalytic and optical properties of such materials. Here, a universal approach for synthesizing metallic open channel superlattices with 10 to 1000 nm pores from DNA-modified hollow colloidal nanoparticles (NPs) is reported. By tuning hollow NP geometry and DNA design, one can adjust crystal pore geometry (pore size and shape) and channel topology (the way in which pores are interconnected). The assembly of hollow NPs is driven by edge-to-edge rather than face-to-face DNA-DNA interactions. Two new design rules describing this assembly regime emerge from these studies and are then used to synthesize 12 open channel superlattices with control over crystal symmetry, channel geometry and topology. The open channels can be selectively occupied by guests of the appropriate size and that are modified with complementary DNA (e.g., Au NPs).

Main Text

Introduction

Porous crystals are a class of materials with extraordinary properties, including high surface areas and low densities, that can be engineered to physically absorb and chemically interact with guest species of known size, shape, and chemical functionality[2–15]. Porous colloidal materials are a particularly interesting class of such structures, as they provide access to inverse photonic structures that can be used for optics, energy storage, and biological applications[16]. These structures are typically made by templating processes[17], a strategy that often relies on face-centered cubic crystals made from spherical particles as templates; this limits the possible pore topologies and distribution of pore volumes.

Although reticular chemical synthesis based upon metal ions and bridging ligand building blocks has led to significant advances in the realization of porous materials (pore apertures < 10 nm), and design rules now exist for the construction of such materials at the molecular scale[18–20], it is still remarkably difficult to prepare porous crystals with customized pore topologies and pore sizes in the range between 10 nm and 1 μm. We hypothesized that three-dimensional (3D) metallic hollow nanoparticles (NPs) [nanoframes (NFs) and nanocages (NCs)] could be assembled into open channel superlattices using colloidal crystal engineering with DNA, an approach that thus far yields access to over 70 different crystal symmetries via well-established design rules based upon the complementary contact model (CCM, the notion that DNA-modified building blocks will arrange themselves in space to maximize complementary interactions)[21–23]. Indeed, consistent with the CCM[23], we determined that the attractive DNA hybridization interactions between the edges of adjacent NFs lead to the formation of ordered superlattices. Notably, this registry-driven edge-to-edge assembly mode (edge-bonding) is distinct from the canonical face-to-face interactions (face-packing) that typically govern the assembly outcomes of solid NPs[24]. It should be noted that an approach that relies on the crystallization of DNA origami subunits[25,26] has been developed, and although this method enables access to certain crystal structures through vertex-to-vertex bonding, it yields structures that are limited in pore dimensions (typical unit size < 50 nm).

Importantly, herein we introduce two new design rules that summarize this edge-bonding construction strategy, through which 12 novel open channel superlattices are synthesized. These structures have symmetries, pore geometries, and topologies that can be deliberately tuned through the choice of hollow NP and DNA. These open channel metallic superlattices not only have the potential to exhibit unnatural optical properties that make them attractive as optical metamaterials but also can be useful for localizing large guests for a variety of applications, including biomolecular absorption and storage, separation, chemical sensing, and catalysis.

Synthesis of open channel superlattices

3D hollow NPs were synthesized in two forms (Fig. 1a): NFs, which represent only the edges of a polyhedron, and NCs, which have some solid faces. Au-Pt NFs were synthesized according to a modified literature procedure[27] from polyhedral Au NPs via a three-step reaction pathway (Fig. 1b-i): 1) edge-selective growth of Pt on Au NPs (Fig. 1b-e); 2) selective etching of Au (Fig. 1f, g), and 3) overgrowth of Au on Pt skeletons (Fig. 1h, i). Using this route, NFs with different shapes (octahedra, triangular prisms, truncated octahedra, cuboctahedra, truncated cubes, and cubes; Fig. 1a and Supplementary Fig.1a-e) and sizes were synthesized. In addition, a novel synthetic route was developed for truncated octahedral, cuboctahedral, and truncated cubic NCs, utilizing a facet-specific growth of Pt on Au NPs method (Supplementary Figs. 1f-h and 2a-d).

The pore sizes of the synthesized NFs and NCs were tailored by changing the growth solution conditions or the sizes of the original NPs utilized (Supplementary Figs. 2e-i and 3a-c). Also, other metallic elements (such as Pd, Rh, Ru, and Ag) can be incorporated into such hollow NPs, if desired, for use in specific applications[28]. For example, Au-Ag NFs were synthesized (Supplementary Fig. 3e) according to literature methods[29].

To assemble these building blocks into superlattices, NFs and NCs were functionalized with self-complementary oligonucleotides (anchor strand A and linker A_2) (Fig. 1j and Supplementary Table 1), such that every particle can hybridize with any other particle in the system. The DNA-functionalized hollow NPs were crystallized into superlattices via slow-cooling, where the temperature of the system was lowered from 65 to 25 °C [30]; this strategy allows the system to reach its lowest free energy configuration (Fig. 1k). These crystals were then analyzed in solution by small angle X-ray scattering (SAXS; Extended Data Fig. 6), and they were also encapsulated in silica[31] or stabilized with Ag^+ [32] (Fig. 1l) to permit their analysis in the solid state by scanning electron microscopy (SEM) and transmission electron microscopy (TEM). Representative nanoparticle building blocks used to form the open channel superlattices were also reconstructed by electron microscopy tomography (Supplementary video 4), and 3D models of the corresponding superlattices were constructed based on these tomography data (Extended Data Fig. 7).

Space-Filling NF Polyhedra

Design rule 1: NFs that derive from space-filling shapes assemble into the corresponding space-filling construction via edge-to-edge assembly (edge-bonding). The CCM for the DNA-mediated assembly of space-filling NPs dictates that the most thermodynamically stable assembly outcome is that which maximizes DNA hybridization[23]. Analogously, we posited that for DNA-functionalized NFs, edge-to-edge contact would maximize DNA hybridization and drive the assembly of these particles into specific crystal structures. Based on geometric considerations, we also noted that the arrangement of space-filling shapes, such as cubes, truncated octahedra, and triangular prisms, into their corresponding space-filling constructions also maximizes edge-to-edge contact. Therefore, we predicted that the edge-bonding-driven assembly of NFs with space-filling shapes would favor the most symmetrical space-filling constructions, in which the faces of the representative polyhedra are registered and completely overlapping with one another, but with open channels dictated by NF voids (Extended Data Fig. 1).

The edge-bonding of cubic NFs serves as an illustrative example (Fig. 2a-d). Cubic NFs assemble into porous simple cubic (*sc*) lattices (Fig. 2a-d), corresponding to the space-filling construction, whereby rectangular channels of different sizes and triangular channels are discerned along different lattice directions (Fig. 2b). This design rule is also validated by the construction of body-centered cubic (*bcc*) lattices (Fig. 2e-h, and Supplementary Fig. 4) via the edge-bonding of truncated octahedral NFs. Three representative channel topologies of the *bcc* lattice are shown along the <111>, <100> and <110> directions of the crystal, with mixtures of periodic triangular, quadrilateral, and hexagonal channels in view (Fig. 2f).

Interestingly, triangular prism NFs assembled into two different open channel superlattices depending on DNA design. When functionalized with short, rigid DNA (Supplementary Table 1, anchor strand A and linker A_1), the triangular prism NFs formed one-dimensional (1D) open columnar structures with a single triangular channel along the column direction (Fig. 2i-l). This structure is analogous to that expected from the assembly of solid triangular nanoprisms[33]. In contrast, when more flexible DNA linkers were used (Supplementary Table 1, anchor strand A and linker A_2), the triangular prism NFs assembled into a 3D interlocked honeycomb (*ih*) lattice

(Fig. 2m-p, and Supplementary Fig. 5), in which there are additional in-plane interactions between the sides of adjacent columns. This observation is consistent with studies from our laboratory that elucidate the influence of linker flexibility on NP assembly[34]. Briefly, when DNA flexibility is increased via the incorporation of polyethylene glycol (PEG) units, the stress of contact between the NPs decreases and intracolumnar side-to-side interactions occur. Moreover, DNA surface functionalization renders the outlined shape of a triangular prism NF similar to that of a truncated bitetrahedral frame (Supplementary Fig. 5), a space-filling shape that corresponds to the *ih* lattice. This example shows that the chemical modularity of oligonucleotides enriches the diversity of open channel superlattices that can be prepared via edge-bonding.

Non-Space-Filling NF Polyhedra

Design rule 2: NFs that outline one shape of a convex space-filling pair can assemble into the corresponding space-filling cocrystal lattice via edge-bonding. There are several pairs of solid polyhedra that co-assemble to fill 3D space. If only one solid polyhedron of these space-filling pairs is assembled into the space-filling construction, the structure is not well-stabilized; the system cannot maximize face-to-face interactions and contains voids and unregistered facets[24,35]. In contrast, edge-bonding of non-space-filling NF polyhedra provides a means to facilitate a stable assembly of colloidal particles into highly porous structures, in which NFs tile along their edges (edge-tiling) and edge-to-edge interactions are maximized. For example, NFs that derive from one shape of a space-filling pair can assemble into the corresponding, stable, space-filling lattice, but with structural voids representing the missing shape of the pair. And, unlike with solid polyhedra, these structural voids, which are geometrically complementary to the shape of the NF building blocks, are uniquely stabilized by maximizing the edge-to-edge interactions between the building blocks (Extended Data Fig. 2).

Octahedra and tetrahedra represent one space-filling pair and co-assemble into a cubic close-packed (*ccp*) structure (Extended Data Fig. 2a). The edge-bonding assembly of only octahedral NFs gives the corresponding dual-shape lattice, the *ccp* structure (Fig. 3a-d, and Extended Data Fig. 2b). This *ccp* lattice with an octahedral habit exhibits triangular channels of different sizes (Fig. 3b), and two sets of tetrahedral voids in alternating orientations (shown in yellow and orange in Fig. 3a). In this lattice, the DNA on every edge of the octahedral NFs is hybridized to the DNA on at least one other edge, maximizing overall edge-to-edge interactions and stabilizing the porous structure as well as its void spaces. This result shows that edge-bonding can give rise to new highly porous and non-dense packed (they have voids in addition to the pores) structures that are nonetheless stable. For example, in terms of symmetry, face-packing of solid octahedra (which favor *bcc* symmetry) and vertex-bonding of octahedral origami subunits (which favor *sc* symmetry) do not result in crystals with *ccp* symmetry[24,36].

This design rule can also be applied to cuboctahedra and square pyramids, which form a space-filling pair with body-centered tetragonal (*bct*) symmetry (Extended Data Fig. 2c). We assembled cuboctahedral NFs into an open-channel, low-symmetry lattice with *bct* symmetry (Fig. 3e-h, Extended Data Fig. 2d, and Supplementary Fig. 7). Compared with cubic lattices (*sc*, *bcc*, and *ccp*), the lower symmetry of the *bct* lattice means that there are two types of <100> and <110> directions with distinct projections that contain triangular and quadrilateral channels (Fig. 3f). In addition to these porous channels, there are two sets of square pyramidal voids with alternating orientations (highlighted in yellow and orange in Fig. 3e).

The generality of this rule also allows the structural outcome of NF assembly to be predicted. Finally, noting that truncated cubes and octahedra also form a complementary space-filling pair (Extended Data Fig. 2e), we hypothesized that the assembly of truncated cubic NFs would yield a lattice with octahedral voids. Indeed, we observed a *sc* structure with a cubic habit and octahedral voids (Fig. 3i-l, Extended Data Fig. 2f, and Supplementary Fig. 8). In this *sc* lattice, channels viewed along different crystal directions exhibit triangular, hexagonal, or octagonal shapes (Fig. 3j). Both the channels and structural voids within the lattice define the pore topology of the assembled crystals. Taken together, these three examples of superlattices assembled via the edge-bonding of a single NF from a space-filling pair support Design Rule 2, and also markedly increase the number and diversity of open channel superlattice symmetries and topologies that can be accessed.

Programming Pore Geometry and Topology

Pore geometry and topology are two important characteristics that determine potential applications. These parameters can be deliberately adjusted by changing the dimensions of the hollow NPs. First, the channel size can be tuned by changing the size and thickness of the NFs (Supplementary Figs. 2, 3a-c, and Extended Data Fig. 3). As a proof-of-concept, we synthesized octahedral NFs with edge lengths of 70, 130, 175, and 250 nm with triangular pores of 30, 75, 90 and 160 nm, respectively. Each of these NFs assembled into superlattices with *ccp* symmetry but with substantially different channel sizes (Fig. 3d, and Extended Data Fig. 3). Note that, in the *ccp* lattice, one of the channel sizes is the same as the particle pore size, but several channels of different sizes exist (Fig. 3b). To illustrate the broad range of pore size tunability through choice of NF building block, we also synthesized octahedral NFs with pores spanning the meso- and macroporous range, specifically, 8, 285 and 1020 nm pores on NFs (Supplementary Fig. 3a-c). In principle, the channel sizes can be readily tuned in the 10 nm to 1 μm range by using particles with different edge lengths and pore sizes.

Second, we show that pore topology can be changed by assembling NFs with specific faces retained, that is, the corresponding NCs (Extended Data Fig. 4). To help visualize the channel topologies of different porous crystals, models of crystals are constructed, in which the volumes occupied by all the pores and channels are filled, and the solid material in the NFs and DNA are removed. Truncated octahedral NFs can be assembled via edge-bonding (Fig. 2e) into crystals with the same symmetry (*bcc*) as those attained when solid truncated octahedral NPs are assembled via face-to-face packing. We therefore hypothesized that a *bcc* lattice with intermediate pore size and different pore topology could be obtained via assembly through the specific-facet registration of truncated octahedral NCs (prepared by selectively retaining the {100} facets of truncated octahedral NFs) (Fig. 4a-d). Indeed, crystals with the same symmetry but with distinct pore topology and dramatically reduced pore size along the <100> direction were obtained when NCs (Fig. 4b) were assembled instead of truncated octahedral NFs (Fig. 2f). Similarly, the channels within *sc* structures assembled from truncated cubic NCs (Fig. 4e-h, and Supplementary Fig. 9) are less open than those in *sc* structures prepared using truncated cubic NFs (Fig. 3i-l).

A similar effect is observed for hollow cuboctahedral NPs, where cuboctahedral NCs with six {100} facets assemble into a *bct* lattice (Fig. 4i-l, and Supplementary Fig. 10), the same structure observed for the edge-bonding of cuboctahedral NFs, but with a different pore topology and reduced pore size. Notably, increasing the flexibility of the DNA attached to the cuboctahedral NCs changes the lattice symmetry (from *bct* to *sc*) with a concomitant change in pore topology and size (Supplementary Fig. 11). Therefore, the pore geometry and topology of the superlattice can be tuned by changing the dimensions of the NFs, by employing NCs where specific facets are solid (compared to NFs), and through judicious DNA design (that also affects lattice symmetry).

Importantly, we can control the pore topology and crystal symmetry independently using these strategies.

By surveying the 12 porous structures discovered here and comparing the projections of their continuous channels along different directions as the crystals grow (simulation in Supplementary Video 1), we see that the channel topology is a function of both the crystal symmetry and the shape of the constituent building block (Extended Data Fig. 5). For example, the four *sc* structures (Extended Data Fig. 5d,f,h,j) obtained via assembly of cubic NFs, truncated cubic NFs, truncated cubic NCs, and cuboctahedral NCs have substantially different channel topologies even though their crystal symmetries are identical. Furthermore, the three *bcc* structures (Extended Data Fig. 5e,g,i) assembled from truncated octahedral NFs and truncated octahedral NCs, and the two *bct* structures (Extended Data Fig. 5k,l) assembled from cuboctahedral NFs and cuboctahedral NCs, all display significantly different channel topologies. Note that even within a single crystal, there are often channels of different shapes and sizes that are highly tailorable. Therefore, building block shape and lattice symmetry provide two design handles for defining the channel topology in nanoscale porous crystals.

Encapsulation of Guests in Open Lattices

As a proof-of-concept test of the open channels inside the assembled crystals, we co-assembled Au nanospheres of different sizes (core diameters of 30 and 20 nm with DNA shell thickness of approximately 7.5 nm) with truncated cubic NFs (edge length of ~100 nm). NFs were functionalized with anchor A/linker A_3 or anchor B/linker B (Fig. 4m, Supplementary Table 1), whereby complementary linkers A_3 and B hybridize to form a *sc* superlattice. Spheres were functionalized with strand B* and thus can hybridize with half of the NFs (those with linker A_3,

Fig. 4n). Both SEM and cross-section TEM images reveal that spheres interact with the assembled truncated cubic NFs and localize selectively in alternating pores of the resulting *sc* lattice (Fig. 4o,p). This selective localization is signified by a characteristic checkerboard pattern for co-crystals with 30 nm spheres (Fig. 4o and Supplementary Fig. 13) and 20 nm spheres (Fig. 4p and Supplementary Fig. 14). These results suggest that one can achieve selective guest localization in the periodic, continuous pores of open channel superlattices through DNA-programmed interactions. Furthermore, assembled superlattices are able to act as host structures, encapsulating guests via post-synthesis diffusion (Supplementary Fig. 15). This capability provides opportunities to design the loading and transport of large guest species that could yield material behaviors not yet achievable in existing porous crystals.

Negative Refractive Index Metamaterials

The controllable and tunable pore topologies and periodicities of open channel superlattices make them promising candidates to realize optical phenomena that are not observed in natural materials. Indeed, negative refractive index materials, structures aggressively pursued by the materials science and physics communities, could become important for super-resolution imaging, cloaking, and other applications[37]. Since these open channel superlattices are reminiscent of split ring resonators, metamaterials known to exhibit negative refractive indices[38], we were curious if this new class of structures could also exhibit negative refraction. Interestingly, optical simulations of a *ccp* crystal (Extended Data Fig. 8, see also Supplementary Information) indeed confirm that it is possible to realize negative refraction with open channel superlattice architectures. Although promising, there are two practical challenges that must be overcome before open channel superlattices can be developed practically as functional negative refractive materials: (a) new fabrication techniques that potentially take advantage of colloidal crystal engineering coupled with top-down lithography methods would be required to mold the open channel superlattices into large-area, single-crystalline films with desired shapes[39], and (b) new NF synthesis strategies for preparing colloidal building blocks consisting of low-loss metals such as aluminum, would increase the transmission of the open channel superlattices, thereby increasing the performance of devices based upon them.

Conclusion

We have presented a new edge-bonding approach to design and synthesize open channel superlattices using hollow NPs with pore sizes over the 10-1000 nm length scale. The DNA-mediated assembly of hollow NPs offers a potential opportunity to construct negative-refractive-index metamaterials from the bottom-up. Looking forward, functional materials (such as quantum dots, proteins, and viruses) can be strategically localized in the open channels, potentially offering routes to composite architectures that could impact a broad range of fields, spanning catalysis, plasmonics, electronics, and biology.

References

1. Kong, L., Zhong, M., Shuang, W., Xu, Y. & Bu, X.-H. Electrochemically active sites inside crystalline porous materials for energy storage and conversion. *Chem. Soc. Rev.* **49**, 2378–2407 (2020).

2. Slater, A. G. & Cooper, A. I. Function-led design of new porous materials. *Science* **348**, aaa8075 (2015).

3. Wang, J. *et al.* New insights into the structure–performance relationships of mesoporous materials in analytical science. *Chem. Soc. Rev.* **47**, 8766–8803 (2018).

4. Geng, K. *et al.* Covalent Organic Frameworks: Design, Synthesis, and Functions. *Chem. Rev.* **120**, 8814–8933 (2020).

5. Lee, J.-S. M. & Cooper, A. I. Advances in Conjugated Microporous Polymers. *Chem. Rev.* **120**, 2171–2214 (2020).

6. Finnefrock, A. C., Ulrich, R., Toombes, G. E. S., Gruner, S. M. & Wiesner, U. The Plumber's Nightmare:1 A New Morphology in Block Copolymer−Ceramic Nanocomposites and Mesoporous Aluminosilicates. *J. Am. Chem. Soc.* **125**, 13084–13093 (2003).

7. Meza, L. R., Das, S. & Greer, J. R. Strong, lightweight, and recoverable three-dimensional ceramic nanolattices. *Science* **345**, 1322 – 1326 (2014).

8. Zhou, J. & Wang, B. Emerging crystalline porous materials as a multifunctional platform for electrochemical energy storage. *Chem. Soc. Rev.* **46**, 6927–6945 (2017).

9. Sun, M.-H. *et al.* Applications of hierarchically structured porous materials from energy

storage and conversion, catalysis, photocatalysis, adsorption, separation, and sensing to biomedicine. *Chem. Soc. Rev.* **45**, 3479–3563 (2016).

10. Vyatskikh, A. *et al.* Additive manufacturing of 3D nano-architected metals. *Nat. Commun.* **9**, 593 (2018).

11. Hirt, L., Reiser, A., Spolenak, R. & Zambelli, T. Additive Manufacturing of Metal Structures at the Micrometer Scale. *Adv. Mater.* **29**, 1604211 (2017).

12. Ullal, C. K. *et al.* Photonic crystals through holographic lithography: Simple cubic, diamond-like, and gyroid-like structures. *Appl. Phys. Lett.* **84**, 5434–5436 (2004).

13. Park, H. & Lee, S. Double Gyroids for Frequency-Isolated Weyl Points in the Visible Regime and Interference Lithographic Design. *ACS Photonics* **7**, 1577–1585 (2020).

14. Phan, A. *et al.* Synthesis, Structure, and Carbon Dioxide Capture Properties of Zeolitic Imidazolate Frameworks. *Acc. Chem. Res.* **43**, 58–67 (2010).

15. Furukawa, H., Cordova, K. E., O'Keeffe, M. & Yaghi, O. M. The Chemistry and Applications of Metal-Organic Frameworks. *Science* **341**, 1230444 (2013).

16. Armstrong, E. & O'Dwyer, C. Artificial opal photonic crystals and inverse opal structures–fundamentals and applications from optics to energy storage. *J. Mater. Chem. C* **3**, 6109–6143 (2015).

17. Hoeven, J. E. S. van der, Shneidman, A. V., Nicolas, N. J. & Aizenberg, J. Evaporation-Induced Self-Assembly of Metal Oxide Inverse Opals: From Synthesis to Applications. *Acc. Chem. Res.* **55**, 1809–1820 (2022).

18. Friedrichs, O. D., Dress, A. W. M., Huson, D. H., Klinowski, J. & Mackay, A. L.

Systematic enumeration of crystalline networks. *Nature* **400**, 644–647 (1999).

19. Yaghi, O. M. *et al.* Reticular synthesis and the design of new materials. *Nature* **423**, 705–714 (2003).

20. Hoffmann, F. *Introduction to crystallography*. (Springer Nature, 2020).

21. Mirkin, C. A., Letsinger, R. L., Mucic, R. C. & Storhoff, J. J. A DNA-based method for rationally assembling nanoparticles into macroscopic materials. *Nature* **382**, 607–609 (1996).

22. Samanta, D., Zhou, W., Ebrahimi, S. B., Petrosko, S. H. & Mirkin, C. A. Programmable Matter: The Nanoparticle Atom and DNA Bond. *Adv. Mater.* **34**, (2022).

23. Macfarlane, R. J. *et al.* Nanoparticle Superlattice Engineering with DNA. *Science* **334**, 204–208 (2011).

24. O'Brien, M. N., Lin, H. X., Girard, M., Olvera De La Cruz, M. & Mirkin, C. A. Programming Colloidal Crystal Habit with Anisotropic Nanoparticle Building Blocks and DNA Bonds. *J. Am. Chem. Soc.* **138**, 14562–14565 (2016).

25. Tian, Y. *et al.* Lattice engineering through nanoparticle–DNA frameworks. *Nat. Mater.* **15**, 654–661 (2016).

26. Zhang, T. *et al.* 3D DNA Origami Crystals. *Adv. Mater.* **30**, 1–6 (2018).

27. Ham, S., Jang, H.-J., Song, Y., Shuford, K. L. & Park, S. Octahedral and Cubic Gold Nanoframes with Platinum Framework. *Angew. Chem. Int. Ed.* **54**, 9025–9028 (2015).

28. Yang, T.-H. *et al.* Noble-Metal Nanoframes and Their Catalytic Applications. *Chem. Rev.* **121**, 796–833 (2021).

29. Wang, Y. *et al.* Synthesis of Silver Octahedra with Controlled Sizes and Optical Properties via Seed-Mediated Growth. *ACS Nano* **7**, 4586–4594 (2013).

30. Auyeung, E. *et al.* DNA-mediated nanoparticle crystallization into Wulff polyhedra. *Nature* **505**, 73–77 (2014).

31. Auyeung, E., Macfarlane, R. J., Choi, C. H. J., Cutler, J. I. & Mirkin, C. A. Transitioning DNA-Engineered Nanoparticle Superlattices from Solution to the Solid State. *Adv. Mater.* **24**, 5181–5186 (2012).

32. Oh, T. *et al.* Stabilization of Colloidal Crystals Engineered with DNA. *Adv. Mater.* **31**, 1805480 (2019).

33. Jones, M. R. *et al.* DNA-nanoparticle superlattices formed from anisotropic building blocks. *Nat. Mater.* **9**, 913–917 (2010).

34. Senesi, A. J. *et al.* Oligonucleotide Flexibility Dictates Crystal Quality in DNA-Programmable Nanoparticle Superlattices. *Adv. Mater.* **26**, 7235–7240 (2014).

35. Gong, J. *et al.* Shape-dependent ordering of gold nanocrystals into large-scale superlattices. *Nat. Commun.* **8**, (2017).

36. Tian, Y. *et al.* Ordered three-dimensional nanomaterials using DNA-prescribed and valence-controlled material voxels. *Nat. Mater.* **19**, 789–796 (2020).

37. Smith, D. R., Pendry, J. B. & Wiltshire, M. C. K. Metamaterials and Negative Refractive Index. *Science* **305**, 788–792 (2004).

38. Shelby, R. A., Smith, D. R. & Schultz, S. Experimental Verification of a Negative Index of Refraction. *Science* **292**, 77–79 (2001).

39. Sun, L. *et al.* Position- and Orientation-Controlled Growth of Wulff-Shaped Colloidal Crystals Engineered with DNA. *Adv. Mater.* **32**, 2005316 (2020).

Figure Legends

Fig. 1| Reaction pathway for the synthesis of hollow NPs (NFs and NCs) and open channel superlattices. a, Models of hollow NPs of different shapes. **b-i**, SEM images and corresponding models of intermediates in the synthesis of Au octahedral NFs, including (**b-e**) octahedral NPs with edge-selective Pt growth, (**f**, **g**) Pt octahedral NFs where the Au content has been selectively etched, and (**h**, **i**) Au-Pt octahedral NFs where Au has been grown on the Pt skeleton. **j-l,** Scheme of the DNA-mediated crystallization and stabilization of open channel superlattices. Octahedral NFs are (**j**) functionalized with DNA, (**k**) slowly annealed from high to low temperature to form crystals, and (**l**) stabilized by encapsulation in silica or by soaking with Ag^+ ions. Scale bars: 100 nm.

Fig. 2| Edge-bonding of NFs that outline space-filling shapes. a-d, Porous crystals with *sc* symmetry assembled from cubic NFs, with models shown in (**a**) perspective view and (**b**) projected along the indicated lattice directions. (**c**) Model showing the pore topology, in which the volumes occupied by all the pores and channels are filled, and the solid material in the NFs and DNA are removed. (**d**) SEM images with different magnifications. **e-h**, Porous crystals with *bcc* symmetry assembled from truncated octahedral NFs, with models shown in (**e**) perspective view and (**f**) projected along the indicated lattice directions. (**g**) Model showing the pore topology. (**h**) SEM images with different magnifications. **i-l**, Porous open columnar structures assembled from triangular prism NFs using short, rigid DNA, with models shown in (**i**) perspective view and (**j**) projected along the indicated directions. (**k**) Model showing the pore topology. (**l**) SEM images with different magnifications. **m-p**, Porous *ih* structures assembled from triangular prism NFs using flexible DNA, with models shown in (**m**) perspective view and (**n**) projected along the indicated directions. (**o**) Model showing the pore topology. (**p**) SEM images with different magnifications. Scale bars: 2.5 µm (SEM images, left) and 500 nm (SEM images, right).

Fig. 3| Edge-bonding of NFs that outline one shape of a space-filling pair. a-d, Porous crystals with *ccp* symmetry assembled from octahedral NFs, with models shown in (**a**) perspective view and (**b**) projected along the indicated lattice directions. In (**a**), the tetrahedral voids are depicted in yellow and orange. (**c**) Model showing the pore topology. (**d**) SEM images with different magnifications. **e-h**, Porous crystals with *bct* symmetry assembled from cuboctahedral NFs, with models shown in (**e**) perspective view and (**f**) projected along the indicated lattice directions. In (**e**), square pyramidal voids are depicted in yellow and orange. (**g**) Model showing the pore topology. (**h**) SEM images with different magnifications. **i-l**, Porous crystals with *sc* symmetry assembled from truncated cubic NFs, with models shown in (**i**) perspective view and (**j**) projected along the indicated lattice directions. In (**i**), octahedral voids are depicted in yellow. (**k**) Model showing the pore topology. (**l**) SEM images with different magnifications. Scale bars: 2.5 µm (SEM images, left) and 500 nm (SEM images, right).

Fig. 4| Adjusting pore topologies of open channel superlattices and encapsulation of guests in open lattices. a-d, Porous crystals with *bcc* symmetry assembled from truncated octahedral NCs, with models shown in (**a**) perspective view and (**b**) projected along the indicated lattice directions. (**c**) Model showing the pore topology. (**d**) SEM images. **e-h**, Porous crystals with *sc* symmetry and cubic habit assembled from truncated cubic NCs, with models shown in (**e**) perspective view and (**f**) projected along the indicated lattice directions. (**g**) Model showing the pore topology. (**h**) SEM images. **i-l**, Porous crystals with *bct* symmetry assembled from cuboctahedral NCs, with models shown in (**i**) perspective view and (**j**) projected along indicated lattice directions. (**k**) Model showing the pore topology. (**l**) SEM images. **m**, Scheme showing co-assembly of Au spheres and truncated cubic NFs. Color denotes DNA design: anchor A/linker A_3 (dark purple) or anchor B/linker B (yellow) or strand B* (light purple). **n**, Model of the co-assembled crystal with *sc* symmetry and cubic habit. **o**, **p**, EM images of the resulting crystals, where (**o**) 30 or (**p**) 20 nm spheres are selectively located in the pores of the open channel superlattices. High-resolution SEM images (top insets) and cross-section TEM images (bottom insets), showing the checkerboard pattern formed by NFs that adsorbed spheres and those that did not. Unless otherwise indicated, scale bars: 2.5 μm (SEM images, left) and 500 nm (SEM images, right); 100 nm (bottom insets of o, p).

Methods

Synthesis of Au-Pt nanoframes and nanocages

Gold triangular nanoprisms were synthesized according to Millstone *et al*.[40] The synthesis of nanoprisms resulted in a significant number of pseudo-spherical nanoparticle (NP) impurities. To isolate the triangular nanoprisms, a depletion force-mediated procedure reported by Young *et al*.[41] was utilized. Briefly, the unpurified nanoprism solution was transferred to 15-ml Falcon tubes and brought to 0.2 M NaCl. After 1 h, this solution was centrifuged for 10 s at 6,000 rpm. The supernatant, containing the pseudo-spherical NP impurities, was removed. The pellet containing triangular nanoprisms was then resuspended in 50 mM CTAB.

Cubic, octahedral, truncated octahedral, cuboctahedral, and truncated cubic gold NPs were synthesized via a literature method[42,43]. In this strategy, iterative oxidative dissolution and reductive growth reactions were utilized to control NP seed structural uniformity. Subsequently, these seeds were used to template the growth of different anisotropic NPs: cubes, octahedra, truncated octahedra, cuboctahedra, and truncated cubes. NPs of larger sizes (> 400 nm) were synthesized through iterative growth.

Gold nanoframes (NFs) of different shapes were synthesized based on a reported pathway[27]. This pathway includes three chemical reactions: 1) edge-selective growth of Pt on Au NPs of different shapes; 2) selective etching of Au; and 3) overgrowth of Au on Pt skeletons to form Au NFs of different shapes, including cubic, triangular prism, truncated cubic, cuboctahedral, and truncated octahedral NFs (Supplementary Fig. 1). First, for the edge-selective growth process to synthesize Au@Pt NPs, 7.5 ml of 50 mM CTAB, 2.5 ml of NP solution, 5 ml of 10 mM $AgNO_3$, and 144 ml of 100 mM ascorbic acid (AA) were added to a vial in the presence of NaI (50 mM). The solution was heated to 70 °C to promote the deposition of Ag layers onto the Au octahedral

NPs. After 1 h, 14.4 ml of 1 M HCl and 40 ml of 16 mM aqueous H_2PtCl_6 solution were injected into the growth solution. The mixture was kept at 70 °C for approximately 3 h. After completion of the reaction, the reaction products were purified from excess reagents via centrifugation for 5 min at 1,500 rcf. The supernatant was removed, and the NPs were resuspended in 10 ml of 50 mM CTAB. Second, to obtain the Pt skeleton, 10 ml of 50 mM CTAB, 60 ml of 25 mM $HAuCl_4$, and Au@Pt NPs were combined in the presence of iodide ions (50 mM). The Au etching step took 2 h at 50 °C. After etching, the products of the reactions were purified from the excess reagents by centrifugation for 5 min at 2,800 rcf. The supernatant was removed, and the Pt skeletons were resuspended in 50 mM CTAB. Finally, to synthesize the Au-Pt NFs, the Pt skeletons were dispersed in 12 ml of CTAB with 50 mM of iodide ions and 12 ml of 1 M HCl, 120 ml of 100 mM AA, 3 ml of 10 mM $AgNO_3$, and 16 ml of 25 mM $HAuCl_4$ was added. To control the pore sizes of the NFs, the volume of Au^{3+} solution was varied from 5 to 60 ml. The pore sizes decrease as more gold atoms are deposited on each frame (Supplementary Fig. 2).

Gold nanocages (NCs) of different shapes were synthesized through a pathway similar to that for the NFs above with slight modifications. The steps involved: 1) edge and specific facet-selective growth of Pt on Au NPs of different shapes; 2) selective etching of Au; and 3) overgrowth of Au on Pt cages to form Au NCs of different shapes, including truncated octahedral, cuboctahedral, and truncated cubic NCs (Supplementary Figs. 1 and 2). Compared to the NF synthesis, in the first step of the NC synthesis, the concentration of the Au NP starting material was half that used for the NF synthesis, and the temperature was 75 ºC. All other conditions were the same.

DNA synthesis and purification

Oligonucleotide sequences were carefully designed for all experiments prior to synthesis (Supplementary Table 1). Oligonucleotides were synthesized on a Mermade 12 (MM12) DNA synthesizer. After synthesis, the oligonucleotides were cleaved from the controlled pore glass (CPG) beads using a solution containing a 1:1 volume mixture of 30% ammonium hydroxide and 40% aqueous methylamine solution (incubation at 55 °C for 30 min). After evaporation, all of the oligonucleotides were purified using reverse-phase high performance liquid chromatography (RP-HPLC) on a Varian Microsorb C18 column (10 μm, 300 × 10 mm). Then, the oligonucleotides were treated with acetic acid solution and ethyl acetate solutions to remove the DMT functional groups. After synthesis and purification, all oligonucleotides were characterized by matrix-assisted laser desorption ionization time-of-flight mass spectrometry (MALDI-TOF-MS) to confirm their molecular mass and purity.

Synthesis of open channel superlattices

All of the synthesized porous NPs, including NFs and NCs, were functionalized with anchor DNA following a literature procedure[23]. First, 3'-propylthiol-terminated anchor strands were incubated with 100 mM dithiothreitol (DTT) for 1 h to cleave the disulfide end. Then, the DTT was removed via size-exclusion chromatography with a NAP25 Column (GE Healthcare). Afterwards, the anchor strands were added to the porous NP suspensions (~8 nmol DNA per ml of porous NPs), and 1 wt% sodium dodecyl sulfate (SDS) and 1 M sodium phosphate (pH = 7.5) were added to reach final concentrations of 0.01 wt% SDS and 10 mM sodium phosphate, respectively. Next, stepwise additions of 5 M NaCl solution (with each aliquot raising the total NaCl concentration by approximately 0.1 M) were added to the solution until it reached a final concentration of 0.5 M NaCl; each addition was followed by 30 s of sonication. This solution was shaken overnight to maximize DNA loading. Excess DNA strands were removed by three rounds of centrifugation/supernatant removal/resuspension. After the final centrifugation step, the anchor-coated porous NPs were redispersed in 0.5 M NaCl buffer (with 0.01 wt% SDS and 10 mM sodium phosphate buffer). Then, 10 nmol of DNA linkers were added to 200 μL of concentrated NP solution. Self-complementary particles are ones with DNA that allow all particles to recognize and hybridize with one another, while complementary systems involve particles with two different but complementary DNA designs. The crystallization was performed through slow-cool annealing with a ProFlex PCR system (Applied Biosystems)[30]. Specifically, the temperature was slowly decreased from 65 ºC to 25 ºC at a rate of 0.01 ºC/min.

Resin embedding of silica embedded crystals and ultramicrotomy

The samples were embedded in a silica/resin following literature methods[24]. Briefly, the silica embedded colloidal crystals were added to 0.2 ml of 4% gelatin. The gelatin sample was dehydrated upon immersion in anhydrous ethanol solutions of increasing concentration (30% → 50% → 70% → 80% → 90% → 100%). Next, the sample immersed in 100% ethanol was solvent-exchanged with acetone twice for 10 min. In acetone, the gelatin was embedded in EMBed-812 resin (Electron Microscopy Sciences) following the standard protocol provided by the manufacturer. The samples were held at 65 °C for 48 h to polymerize and solidify the resin, and the resin was then sectioned into 100-nm slices (Leica EM UC7).

Characterization

These crystals were analyzed in solution by small angle X-ray scattering (SAXS); and in the solid state, after encapsulation in silica or stabilization with Ag^+, with scanning electron microscopy (SEM)[31,32]. These two methods allow one to transfer open channel superlattices in the assembled state and preserve crystal symmetry for imaging. To characterize the inner-guest distribution of the crystals, the silica-stabilized crystals were subsequently embedded in a resin and cross-sectioned to image the interior structure.

3D reconstruction

The tilt series high angle annular dark field (HAADF) images were collected using a JEOL ARM 200CF microscope, operated at 200 kV. This microscope was equipped with a probe corrector, and the spatial resolution in scanning transmission electron microscope (STEM) mode is about 0.8 Å. The convergence angle used was 30 mrad. The collection angle of HAADF imaging ranged from 90 to 250 mrad. The tilt series were collected manually from -70° to + 70° at 2° increments. All tilt series were initially aligned using the IMOD software package[44]. For the final 3D reconstruction (Supplementary Video 4), we used the MBIR method[45].

Optical simulation of open channel superlattices

Full electromagnetic simulations were performed using commercial software, Ansys Lumerical Finite Difference Time Domain (FDTD). The core diameter, shell diameter, and edge length of the NFs, and interparticle gap between adjacent NFs were taken as 17 nm, 30 nm, 160 nm, and 10 nm, respectively. The NFs were embedded into SiO_2 (n=1.45). Johnson-and-Christy's model[46] and Werner's model[47] were used as material model for Au and Pt, respectively. The transverse electromagnetic polarized plane wave source was located at (0, 0, 1700 nm) propagating toward the +z direction. The structure was located at the origin "(0, 0, 0)". The S-parameters were taken from 2D/z-normal near-field monitors located in the front ($z < 0$) and back ($z > 0$) of the structure. Simulated phase propagation movies inside the porous *ccp* structure show negative phase propagation inside the material (Supplementary Videos 2 and 3).

Data availability

All data are available in the main Article and Supplementary Information, or from the corresponding authors on request.

Additional References

40. Millstone, J. E., Wei, W., Jones, M. R., Yoo, H. & Mirkin, C. A. Iodide Ions Control Seed-Mediated Growth of Anisotropic Gold Nanoparticles. *Nano Lett.* **8**, 2526–2529 (2008).

41. Young, K. L. *et al.* Assembly of reconfigurable one-dimensional colloidal superlattices due to a synergy of fundamental nanoscale forces. *Proc. Natl. Acad. Sci.* **109**, 2240–2245 (2012).

42. O'Brien, M. N., Jones, M. R., Brown, K. A. & Mirkin, C. A. Universal Noble Metal Nanoparticle Seeds Realized Through Iterative Reductive Growth and Oxidative Dissolution Reactions. *J. Am. Chem. Soc.* **136**, 7603–7606 (2014).

43. Li, Y. *et al.* Corner-, edge-, and facet-controlled growth of nanocrystals. *Sci. Adv.* **7**, eabf1410 (2021).

44. Kremer, J. R., Mastronarde, D. N. & McIntosh, J. R. Computer Visualization of Three-Dimensional Image Data Using IMOD. *J. Struct. Biol.* **116**, 71–76 (1996).

45. Yan, R., Venkatakrishnan, S. V, Liu, J., Bouman, C. A. & Jiang, W. MBIR: A cryo-ET 3D reconstruction method that effectively minimizes missing wedge artifacts and restores missing information. *J. Struct. Biol.* **206**, 183–192 (2019).

46. Johnson, P. B. & Christy, R. W. Optical Constants of the Noble Metals. *Phys. Rev. B* **6**,

4370–4379 (1972).

47. Werner, W. S. M., Glantschnig, K. & Ambrosch-Draxl, C. Optical Constants and Inelastic Electron-Scattering Data for 17 Elemental Metals. *J. Phys. Chem. Ref. Data* **38**, 1013–1092 (2009).

Acknowledgments

We acknowledge S. H. Petrosko [Northwestern University (NU)] for providing editorial input, E. W. Roth (NU) for ultramicrotomy, and S. Krishnaswamy (NU) for providing the NIR laser. This material is based upon work supported by the Air Force Office of Scientific Research under awards FA9550-17-1-0348 (hollow nanoparticle synthesis and DNA functionalization) and FA9550-16-1-0150 (SEM characterization and optical simulation), and the Center for Bio-Inspired Energy Science, an Energy Frontier Research Center funded by the U.S. Department of Energy, Office of Science, Basic Energy Sciences under award DE-SC0000989 (assembly of hollow nanoparticles). X-ray experiments were carried out at beamlines sector 12-ID-B and the DuPont-Northwestern-Dow Collaborative Access Team (DND-CAT) sector 5 of the Advanced Photon Source (APS) (DOE DE-AC02-06CH11357). This work made use of the EPIC facility of Northwestern University's NU*ANCE* Center, which has received support from the Soft and Hybrid Nanotechnology Experimental (SHyNE) Resource (NSF ECCS-2025633); the MRSEC program (NSF DMR-1720139) at the Materials Research Center; the International Institute for Nanotechnology (IIN); the Keck Foundation; and the State of Illinois, through the IIN.

Conflict of interests

The authors declare no competing interests.

Author contributions

Y.L. designed and performed experiments and analyzed the data. W.Z. performed experiments and analyzed the data. I.T. and W.H. did the optical simulation. X.H. and J.L. performed the 3D reconstruction. B.L. performed the SAXS simulations. C.A.M. and K.A. supervised the project. Y.L. wrote the initial draft. Y.L., W.Z., B.E.P., H.L., I.T., W.H., X.H., B.L., J.L., V.P.D., K.A., and C.A.M. all analyzed the data, interpreted the data, and contributed to the writing of the manuscript.

Additional Information

Supplementary Information is available for this paper. Correspondence and requests for materials should be addressed to chadnano@northwestern.edu; aydin@northwestern.edu.

Extended Data Figure Legends

Extended Data Fig. 1 Edge-bonding of NFs and face-packing of solid NPs that outline space-filling shapes. a, Models of *sc* crystals assembled from cubic NFs. **b,** Models of *sc* crystals constructed from solid cubes. **c**, Models of *bcc* crystals assembled from truncated octahedral NFs. **d**, Models of *bcc* crystals constructed from solid truncated octahedra. **e**, Schematic showing that when the building blocks are derived from space-filling shapes (e.g., cubic, truncated octahedral, and triangular prism NFs), maximizing area sharing maximizes edge sharing at the same time, which drives the thermodynamically stable structure based on CCM. Therefore, NFs that derive from space-filling shapes assemble into the corresponding space-filling construction via edge-bonding. Note that the solid cases are built based on the uniform tessellation of polyhedra.

Extended Data Fig. 2 Edge-bonding of NFs that outline one shape of a space-filling pair a, Octahedra and tetrahedra represent one space-filling pair for *ccp* symmetry. **b**, The edge-bonding assembly of only octahedral NFs gives the corresponding dual-shape lattice, the *ccp* structure, with triangular channels of different sizes, and two sets of tetrahedral voids in alternating orientations (shown in yellow and orange). **c**, Cuboctahedra and square pyramids form a space-filling pair for *bct* symmetry. **d**, The edge-bonding assembly of only cuboctahedral NFs gives the corresponding dual-shape lattice, the *bct* structure, with quadrilateral and triangular channels, and two sets of square pyramidal voids with alternating orientations (highlighted in yellow and orange). **e**, Truncated cubes and octahedra form a space-filling pair for *sc* symmetry. **f**, The edge-bonding assembly of only truncated cubic NFs gives the corresponding dual-shape lattice, the *sc* structure, with triangular, hexagonal, and octagonal channels, and octahedral voids (highlighted in yellow). Therefore, NFs that outline one shape of a convex space-filling pair can assemble into the corresponding space-filling cocrystal lattice via edge-bonding. Note that the solid cases are built based on uniform tessellation of polyhedra.

Extended Data Fig. 3 Pore sizes can be deliberately tailored by changing the dimensions of the hollow NP building blocks. a-i, Open channel superlattices with *ccp* symmetry and different channel sizes. Models **(a, d, g)** and SEM images **(b, c, e, f, h, i)** of *ccp* crystals assembled from Au-Pt octahedral NFs in different sizes. Scale bars: 200 nm **(c, f, i)**; 5 μm **(b, e, h)**. L: NF size; l: pore size.

Extended Data Fig. 4 The pore geometry and topology of the superlattices can be tuned by employing NCs where specific facets are solid (compared to NFs). a,b, Models of *bcc* crystals assembled from truncated octahedral NFs and NCs, respectively. **c,d,** Models of *sc* crystals assembled from truncated cubic NFs and NCs respectively. **e,f,** Models of *bct* crystals assembled from cubcotahedral NFs and NCs, respectively. From left to right, each panel contains models showing the building blocks, the assembled porous crystals, and the pore topologies of the corresponding crystals.

Extended Data Fig. 5 Pore topologies are programmed by both the shape of the building blocks and the crystal symmetry. a-l, A library of open channel superlattices include: (**a**) 1D chain assembled from triangular prism NFs; (**b**) *ih* crystal assembled from triangular prism NFs; (**c**) *ccp* crystal assembled from octahedral NFs; (**d**) *sc* crystal assembled form cubic NFs; (**e**) *bcc* crystal assembled from truncated cubic NCs; (**f**) *sc* crystal assembled from cuboctahedral NCs; (**g**) *bcc* crystal assembled from truncated octahedral NFs; (**h**) *sc* crystal assembled from truncated cubic NFs; (**i**) *bcc* crystal assembled from slightly truncated octahedral NCs; (**j**) *sc* crystal assembled from truncated cubic NCs; (**k**) *bct* crystal assembled from cuboctahedral NFs; and (**l**) *bct* crystal assembled from cuboctahedral NCs. From left to right, each panel contains models shown in perspective view, projected along the indicated lattice directions [including <111>, <100> and <110> directions (c-j); <001>, <011>, <111>, <100>, and <110> directions (k-l)], and models showing the pore topologies.

Extended Data Fig. 6 a-h, Experimental (red) and simulated (black) SAXS profiles of open channel superlattices with different symmetries, including (**a**) porous crystals with *sc* symmetry assembled from cubic NFs, (**b**) porous crystals with *bcc* symmetry assembled from truncated octahedral NFs, (**c**) porous crystals with *ccp* symmetry assembled from octahedral NFs, (**d**) porous crystals with *bct* symmetry assembled from cuboctahedral NFs, (**e**) porous crystals with *sc* symmetry assembled from cuboctahedral NCs, (**f**) porous crystals with *bcc* symmetry assembled from truncated octahedral NCs, (**g**) porous crystals with *sc* symmetry assembled from truncated cubic NCs, (**h**) porous crystals with *bct* symmetry assembled from cuboctahedral NCs, and (**i**) porous crystals with *sc* symmetry assembled from truncated cubic NFs. It is worth noting that the signal of the peaks is not strong due to the porous and anisotropic nature of the crystals.

Extended Data Fig. 7 a-b, Reconstructed 3D models of open channel superlattices from electron microscopy tomography. (**a**) Porous crystals with *ccp* symmetry assembled from octahedral NFs viewed from different angles. (**b**) Porous crystals with *bct* symmetry assembled from cuboctahedral NFs viewed from different angles. Tomographic reconstruction is consistent with symmetry considerations.

Extended Data Fig. 8 Negative effective index simulation of the porous *ccp* crystal assembled from Au-Pt octahedral NFs. a, Calculated effective refractive index (*n*, blue line) and extinction coefficient (*k*, red line) of a porous Au-Pt *ccp* crystal. **b**, Electric field phase accumulated throughout the Au-Pt *ccp* crystal at wavelengths corresponding to positive (blue line), near-zero (red line), and negative index (black and purple lines) regions.

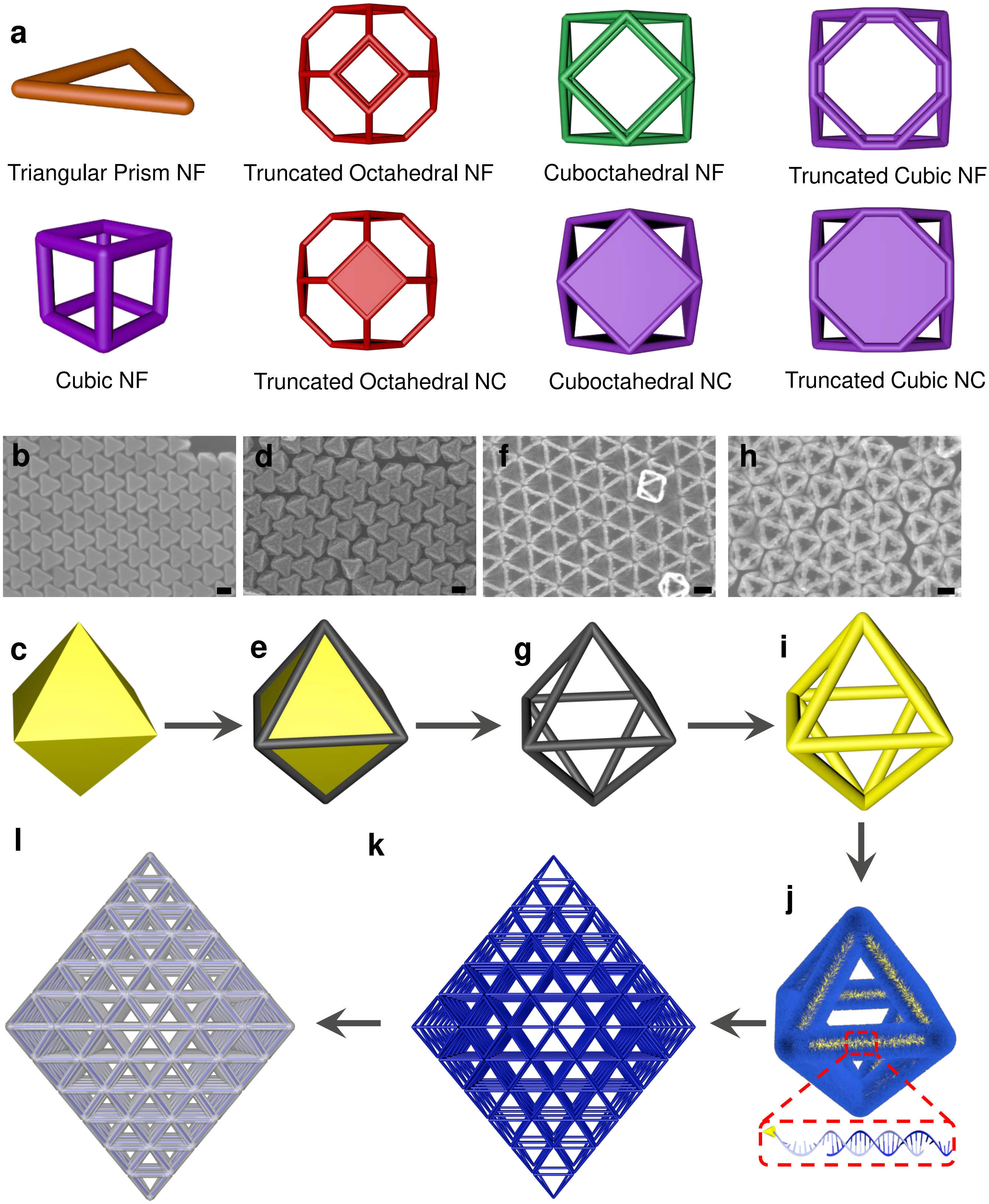
a
Triangular Prism NF
Truncated Octahedral NF
Cuboctahedral NF
Truncated Cubic NF
Cubic NF
Truncated Octahedral NC
Cuboctahedral NC
Truncated Cubic NC
b
d
f
h
c
e
g
i
l
k
j

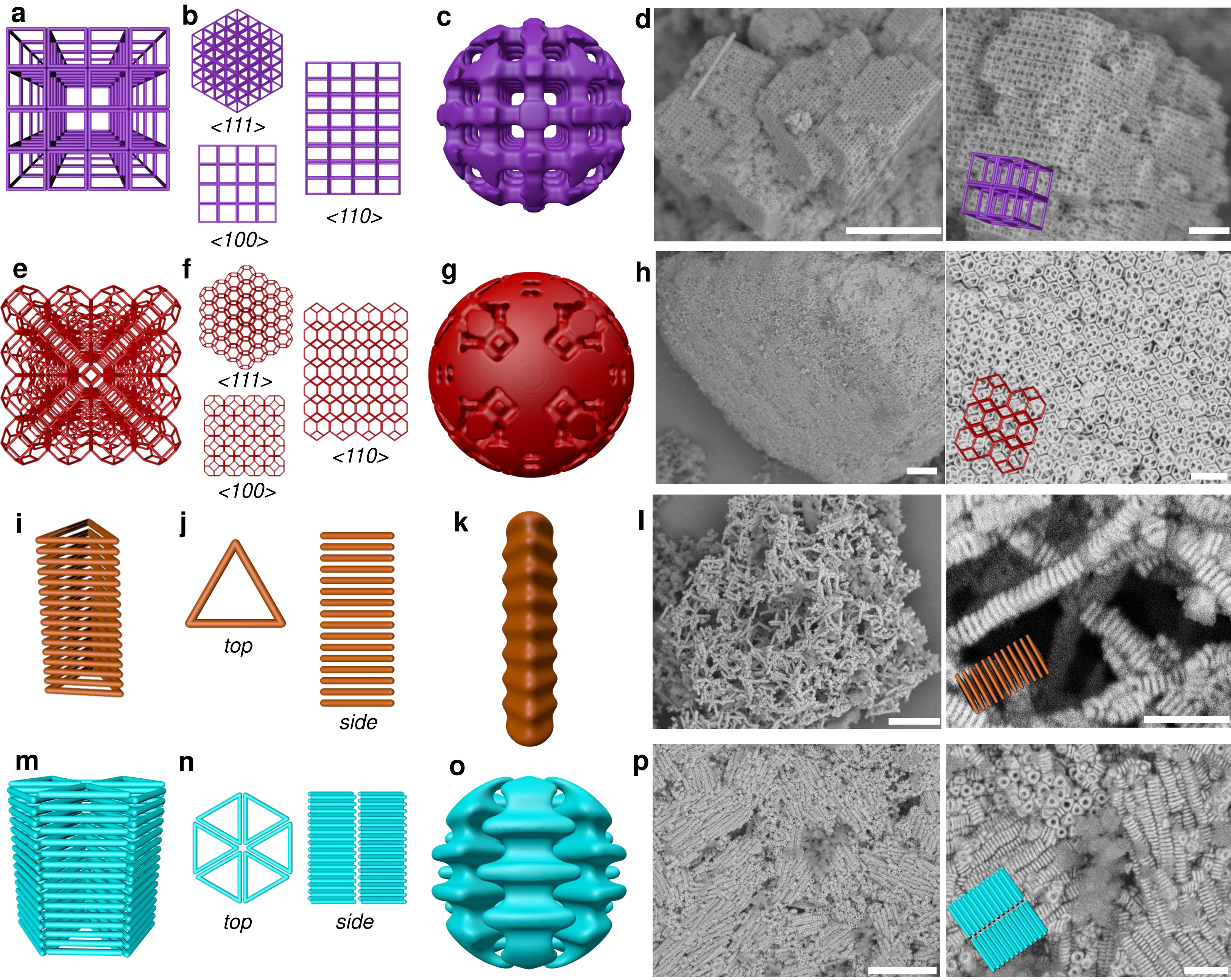

a
b
<111>
<100>
<110>
c
d
e
f
<111>
<100>
<110>
g
h
i
j
top
side
k
l
m
n
top
side
o
p

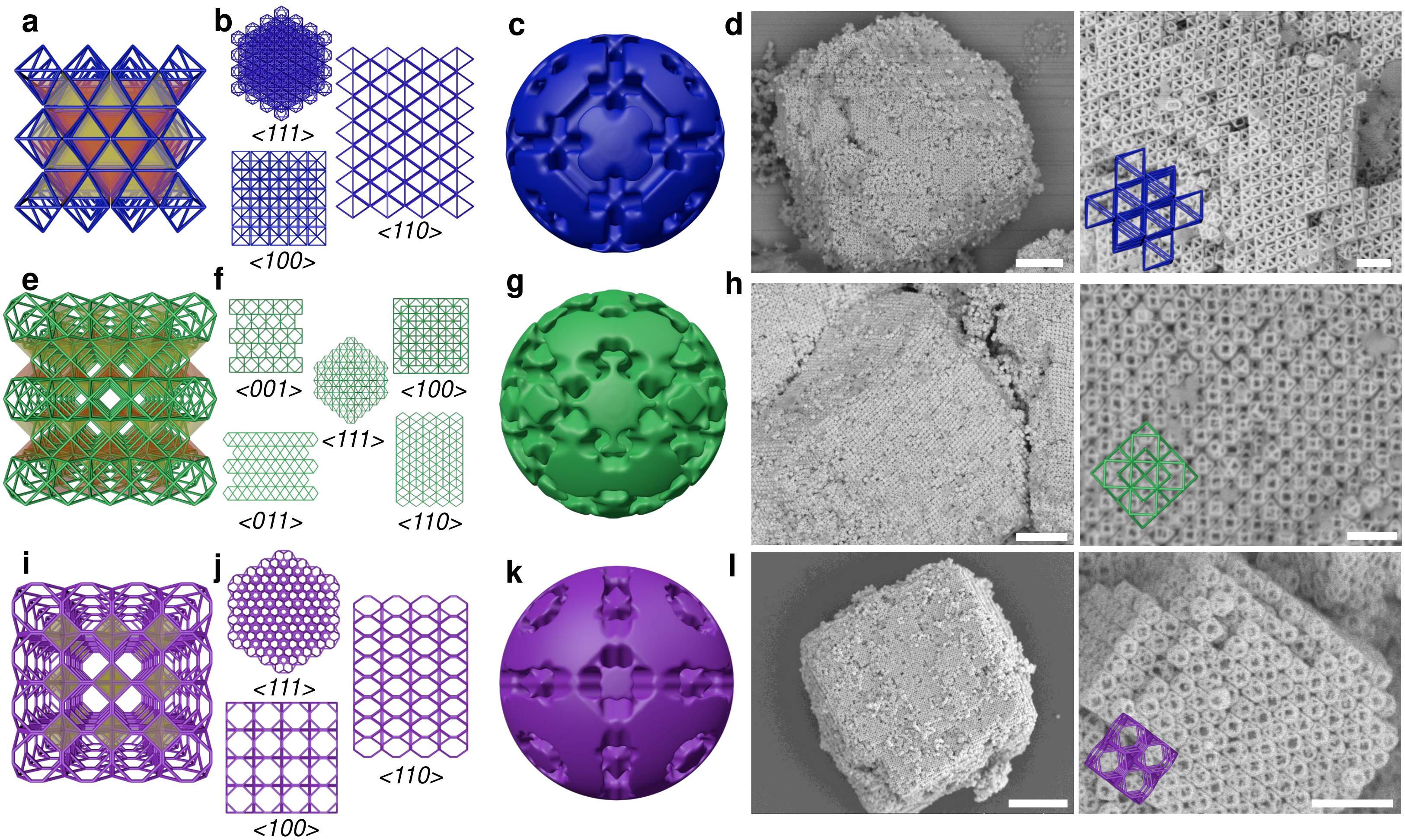

a
b
<111>
<100>
<110>
c
d
e
f
<001>
<111>
<100>
<011>
<110>
g
h
i
j
<111>
<100>
<110>
k
l

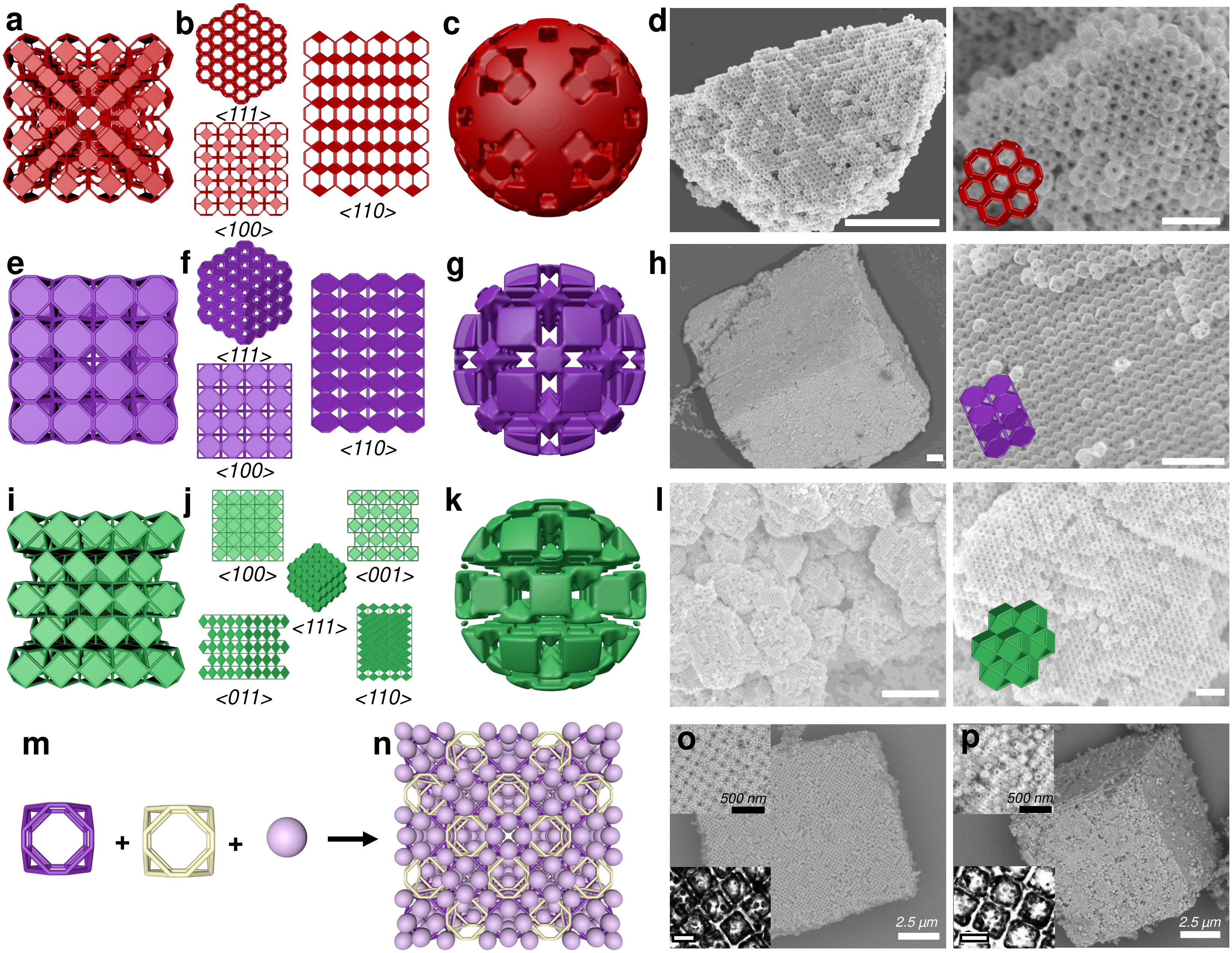

a
b
<111>
<100>
<110>
c
d
e
f
<111>
<100>
<110>
g
h
i
j
<100>
<001>
<111>
<011>
<110>
k
l
m
+
+
n
o
500 nm
2.5 μm
p
500 nm
2.5 μm